Journal of Materials Chemistry A

Accepted Manuscript

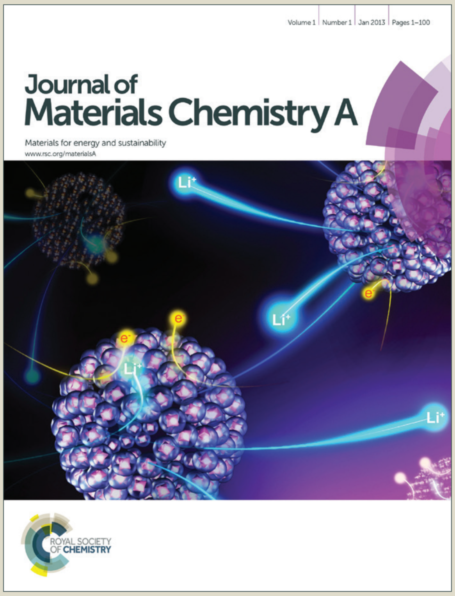

ROYAL SOCIETY OF CHEMISTRY

www.rsc.org/materialsA

A Core–Shell-Structured TiO_2 (B) nanofiber @ porous RuO_2 Composite as a Carbon-Free Catalytic Cathode for Li−O_2 Battery†

Ziyang Guo, Chao Li, Jingyuan Liu, Xiuli Su, Yonggang Wang and Yongyao Xia*

Department of Chemistry and Shanghai Key Laboratory of Molecular Catalysis and Innovative Materials, Institute of New Energy, iChEM(Collaborative Innovation Center of Chemistry for Energy Materials), Fudan University, Shanghai 200433, China. * Corresponding author. Tel & Fax: 0086-21-51630318
E-mail address: *ygwang@fudan.edu.cn*

Keywords: (Li–O_2 battery, Carbon-free cathodes, TiO_2 (B) nanofiber@ porous RuO_2 composite, RuO_2-coating)

Abstract: Porous carbon, which ever is the most widely used cathode material for Li–O_2 batteries, is found to decompose in charging process, promote electrolyte decomposition, and react with the discharge product. Carbon-free cathodes thus become critical for Li–O_2 battery, but generally exhibit low capacity and poor rate because of their high density and pores-insufficient characteristic. Herein, we present a simple method to prepare a core-shell-structured TiO_2 (B) nanofiber@ porous RuO_2 composite, which then is used as a carbon-free catalyst for Li–O_2 battery. The RuO_2 coating layer replicates the structure of TiO_2 nanofiber to form a one dimensional RuO_2 shell with typical hierarchical mesoporous/macroporous structure. Besides the reduced undesired decomposition, the abundant porous structure and inherent high conductivity of RuO_2 coating layer also increase specific capacity, efficiency, rate ability and cycle life. With the high mass loading of 2.5 mg cm^{-2} on cathode, the Li–O_2 battery shows the performance superior to previous reports, including high capacity (800 mAh g^{-1} at a current density of 0.125 mA cm^{-2} or 50 mA g^{-1}) with a very high energy efficiency of >82.5%, good rate (500 mAh g^{-1} at a current density of 0.5 mA cm^{-2} or 200 mA g^{-1}) and long-life (80 cycles at a fixed capacity of 300 mAh g^{-1}). It is also demonstrated that the lithiation/de-lithiation of RuO_2 can contribute capacity over charge/discharge process, indicating that battery can be operated as a rechargeable RuO_2/Li battery without O_2 in environment.

Introduction

Li–O_2 batteries have recently attracted extensive attention because of their extremely high energy potentiality (up to 2–3 kWh kg^{-1}) which is about 5–10 times more energy than current Li-ion batteries. [1-11] However, the development of Li–O_2 batteries is still constrained by several serious challenges. [12, 13] One of the major challenges is that the highly reactive intermediate species of oxygen reduction reaction that form at the cathode attack the electrolyte and cathode, resulting in irreversible side reactions that compromise the reversible formation/decomposition of Li_2O_2 on cycling.[14-21] Concerning electrolyte stability, it is now widely recognized that many commonly used organic carbonate based electrolytes suffer severe decomposition at the cathode during cycles.[14, 15, 22, 23] Later work turned to ether [6, 7, 10, 24-31] and dimethylsulfoxide (DMSO) based electrolytes [8, 9, 11, 32] since they have been demonstrated to be relatively robust electrolytes for non-aqueous Li–O_2 batteries, though completely stable electrolytes are still lacking. Another serious problem for rechargeable Li–O_2 batteries is cathode. Carbon is the most widely used cathode material for Li–O_2 cells because it possesses many critical factors, including large surface area, low mass, high conductivity and highly porous structure.[7, 25-27, 31, 33-45] However, it was demonstrated recently that carbon decomposes at certain potentials in the charging process, promotes the decomposition of electrolytes during discharge and charge, and reacts with the discharge product Li_2O_2.[16, 20, 32] Therefore, it is quite necessary to develop alternative cathodes.

In recent two years, some investigations have focused on carbon-free cathodes for

Li–O_2 batteries.[8, 9 46-53] However, owing to the high density and pores-insufficient characteristic compared with carbon-based cathode, these carbon-free cathodes generally exhibit low capacity and poor rate. The first attempt of carbon-free cathode for Li–O_2 battery was made by Bruce's group on a nanoporous gold (NPG) combined with a DMSO-based electrolyte. Although this cell showed good cycling stability, the achieved capacity is only around 320 mAh g^{-1}.[8] Bruce and his co-workers also found that a TiC-based cathode reduced greatly side reactions and exhibited perfect cycle performance due to the thin layer of TiO_2 formed on the surface of TiC. However, the delivered specific capacity was still limited.[9] Different from these two materials, a stable conductive indium tin oxide (ITO) electrode embedded with Ru nanoparticles was first introduced as a carbon-free cathode in Li–O_2 batteries by Zhou's group.[46] A good cycling stability was obtained, but, similar to NPG, ITO is heavy which leads to a low specific capacity per unit mass. Very recently, some efforts were made to increase the specific gravimetric capacity of carbon-free cathode by reducing the mass loading of active materials.[49-53] Although this way can efficiently increase the specific capacity (mAh g^{-1}) that is calculated with the mass of active materials in cathode, the low mass loading much limits the specific areal capacity (mAh cm^{-2}). For example, it has been reported that Ru-based carbon-free cathode can achieve the enhanced capacity (1000 ~ 4000 mAh g^{-1}) with low mass loading of 0.1 ~ 0.15 mg cm^{-2},[50, 53] but the corresponding specific areal capacity (0.1 ~ 0.6 mAh cm^{-2}) is far away from that of conventional Li-ion batteries (2-3 mAh cm^{-2}), which still much limits the practical application of Li–O_2 batteries. Accordingly, achieving the high specific capacity (mAh g^{-1}) with the suitable mass loading was one of the greatest challenges for the Li–O_2 cells.

Here we designed and synthesized core-shell-structured TiO_2 (B) nanofiber@ porous RuO_2 composite by a simple sol-gel method, which features a TiO_2 (B) nanofiber core and a porous RuO_2 shell, as a cathode material for Li–O_2 battery. The typical hierarchical mesoporous/macroporous structure in TiO_2 (B) nanofiber@ porous RuO_2 composites can not only facilitate electrolyte penetration and electron/ion transfer, but also provide efficient buffer space for O_2/Li_2O_2 conversion and improve O_2 diffusion. Moreover, the uniform RuO_2 coating layer alleviates undesired electrolyte and/or electrode decomposition and also improves the surface electronic conductivity. As a result, with a high mass loading of 2.5 mg cm^{-2}, the Li–O_2 battery with the TiO_2 (B) nanofiber@ porous RuO_2 catalytic cathode exhibits good performance, including high capacity with a high energy efficiency, good rate and long life. Furthermore, the TiO_2 (B) nanofiber@ porous RuO_2 composites could act not only as a catalyst to enhance the electrocatalytic activity of rechargeable Li–O_2 cells, but also as a cathode material in Li-ion battery due to the lithiation/de-lithiation of RuO_2, indicating that battery can be operated as a rechargeable RuO_2/Li battery without O_2 in environment.

Experimental Section

Material synthesis

TiO_2 (B)@ RuO_2 was prepared by a sol-gel method. First, the TiO_2 (B) nanofibers were prepared according to our previous strategy. [54] TiO_2 (B) nanofibers (100 mg) were then dispersed in a 0.1 M $RuCl_3$ (30 mL) solution by ultrasonication for 5 min. A 0.3 M $NaHCO_3$ aqueous solution was added slowly to the above mixture under stirring until the pH of the solution reached 7. After another 15 h of stirring, the sediments were washed several times with distilled water, and then dried in air flow at room temperature for 10 h. The black powder thus obtained was annealed at 150°C for 19 h in air and donated as TiO_2 (B) nanofiber@ porous RuO_2. The wt % of RuO_2 coating layer, calculated from the mass difference between the target product (i.e. TiO_2 (B) nanofiber@ porous RuO_2) and the precursor (i.e. TiO_2 (B) nanofiber bundles), is 75 wt% in this composite. The TiO_2 (B) nanofiber@ porous RuO_2 with a RuO_2 content of 75 wt % in this study is abbreviated as “TiO_2 (B)@ RuO_2-75” in the following text. The TiO_2 (B) nanofiber@ RuO_2 composite with a RuO_2 content of 50 wt% was also prepared with the same way for comparison (or TiO_2 (B)@ RuO_2-50, for short). The preparation of TiO_2 (B) nanofibers and pure RuO_2 nanoparticles is given in supporting information.

Material characterization

X-ray diffraction (XRD) measurements were performed on a Bruker D8 Focus power X-ray diffractometer with Cu K radiation. Field emission scanning electron microscopy (SEM) was conducted using a JSM-6390 microscope from JEOL. Transmission electron microscopy (TEM) experiments were conducted using a JEOL 2011 microscope (Japan) operated at 200 kV. Fourier transform-infrared spectroscopy (FT-IR) tests were performed on a Nicolet 6700 spectrometer. Nitrogen sorption isotherms were measured at 77 K with a Micromeritics Tristar 3000 analyzer (USA). Specific surface areas were calculated by the Brunaure– Emmert–Teller method. Pore volumes and sizes were estimated from the pore-size distribution curves from the adsorption isotherms using the Barrett–Joyner– Halenda method. X-ray photoelectron spectroscopy (XPS) was conducted with a Thermo Escalab 250 equipped with a hemispherical analyzer and using an aluminum anode as a source. Power electronic conductivity investigation at the pressure of 4 MPa was performed on a 4-pole conductivity instrument for powder materials (Powder Resistivity Meter, FZ-2010, Changbao Analysis Co., Ltd, Shanghai, China).

Electrochemical Measurement

O_2 catalytic cathode preparation: In the preparation of TiO_2 (B)@ RuO_2-75 catalytic electrode, 80 wt % TiO_2 (B)@ RuO_2-75 and 20 wt % poly (tetrafluoroethylene) (PTFE) binder were intimately mixed in an isopropanol solution, and the resulting slurry was rolled into a membrane, and then pressed on pellets of 12mm in diameter which were pressed onto titanium meshes and worked as cathodes. The mass loading of TiO_2 (B)@ RuO_2-75 is about 2.5mg cm^{-2}. TiO_2 (B) nanofibers, TiO_2 (B)@ RuO_2-50, RuO_2 nanoparticles and KB (Ketjenblack EC600JD produced purchased from Shanghai Tengmin Industry Co., Ltd.) were also employed to prepare the catalytic electrode at the same condition for comparison.

Li–O_2 batteries fabrication and electrochemical measurements: The batteries assembly was operated in a glove box filled with pure argon. Newly polished lithium metal foils were kept in 0.1M $LiClO_4$-propylene carbonate (PC) electrolyte for at least 3 days before being used as the anode in a Li–O_2 cell containing a 0.1 M $LiClO_4$-DMSO electrolyte. This procedure was found to be effective in stabilizing the lithium metal, permitting cycling in DMSO. [8] O_2 catalytic cathode and prepared Li anode were separated by a separator dipping with DMSO-(0.1M) $LiClO_4$ electrolyte. This Li/separator/O_2 cathode was then sealed into a Swagelok cell with an air hole 0.8 cm^2 placed on the positive electrode side to allow the oxygen to flow in. Galvanostatic charge-discharge measurements of these Li–O_2 batteries were carried out in a pure/dry oxygen-filled glove box. LAND cycler (Wuhan Land Electronic Co. Ltd) was employed for electrochemical tests. A quadrupole mass spectrometer (NETZSCH QMS 403 C) with leak inlet was connected to a customized Swagelok cell assembly for DEMS (Differential Electrochemical Mass Spectrometry) investigation (see supporting information for detail). All of the results for the specific capacities and current densities were calculated with the mass loading of TiO_2 (B)@ RuO_2 in the O_2 cathodes.

Results and Discussion

The XRD pattern of TiO_2 (B)@ RuO_2-75, compared with TiO_2 (B) nanofibers, TiO_2 (B)@ RuO_2-50, RuO_2 nanoparticles, is shown in Fig. 1. Specifically, all of the main diffraction peaks in Fig. 1a are attributed to the TiO_2-B, indicating good crystallinity of the pristine TiO_2 (B) nanofibers. As shown in Fig. 1b, the diffraction peaks of TiO_2-B still exist and their intensity is close to that of pristine TiO_2 (B) nanofibers, suggesting that the coating of RuO_2 nanoparticles on the surface of TiO_2

(B)@ RuO_2-50 is limited and most of TiO_2 (B) nanofibers surface is exposed. On the contrary, Fig. 1c presents that only a part of the diffraction peaks for TiO_2-B are still visible and sharply decreased, indicating that the RuO_2 nanoparticles are uniformly coated over the TiO_2 (B) nanofibers surface for TiO_2 (B)@ RuO_2-75. In addition, the two broad peaks appeared at around 32° and 54° in Fig. 1c, which also are observed in the XRD pattern for RuO_2 nanoparticles (Fig. 1d), are assigned to RuO_2.

The as-prepared TiO_2 (B) nanofibers showed a bundle-like microstructure with diameters of about 250nm (see the SEM and TEM images of the pristine-TiO_2 (B) nanofibers in Fig. S1†), and the observed bundle-like microstructure is constructed with a lot of TiO_2-nanofibers with a typical size of about 30~50nm in diameter. When the TiO_2 (B) nanofibers are coated with RuO_2 nanoparticles, the surface became rough (see Fig. 2a and b). But it can be observed from Fig. 2a that bundle-like structure was maintained well in the prepared TiO_2 (B)@ RuO_2-75, indicating that the RuO_2-coating does not destroy the bundle-like structure of supporter of TiO_2 (B) nanofibers. SEM images with higher magnifications indicate that RuO_2 particles with a size of 10 ~ 30 nm, which is the same as the diameter of the pristine RuO_2 naoparticles (Fig. S2†), were evenly distributed on the surface of TiO_2 (B) nanofibers (Fig. 2b). Moreover, it seems that the surface coating layer of TiO_2 (B)@ RuO_2-75 also show a porous structure (see Fig. 2b). However, for TiO_2 (B)@ RuO_2-50, only a fraction of TiO_2 (B) nanofibers are decorated homogeneously with RuO_2 particles, and many RuO_2 nanoparticles agglomerate together, which makes the composite heterogeneous (Fig. S3†). This result is in agreement with the XRD pattern for TiO_2 (B)@ RuO_2-50. Fig.

2c~f shows the TEM images of TiO_2 (B)@ RuO_2-75 which are consistent with the SEM observation. The TEM images (Fig. 2c and d) further shows that the RuO_2 nanoparticles are uniformly distributed over the TiO_2 (B) nanofibers surface. Furthermore, it can be detected from Fig. 2c, d and Fig. S1† that the diameter of the resulting composite TiO_2 (B)@ RuO_2-75 had increased to about 350 nm from ~250 nm in the pristine TiO_2(B) nanofibers. In the enlarged TEM images (Fig. 2e and f), the RuO_2 nanoparticles with crystal lattices can also be detected clearly in some areas, which are obviously different from the crystalline structure of TiO_2 (B) nanofibers (Fig. S1d†). We also used energy-dispersive X-ray (EDX) mapping to further investigate the distribution and composition of TiO_2 (B)@ RuO_2-75 composite. TEM image of the composition and EDX mapping of elements Ru, Ti and O are shown in Fig. 2g-l. The Ti element is distributed as a rod-like structure with a diameter of ~250 nm, which is in agreement with the diameter of the TiO_2 (B) nanofibers (see Fig. 2i and Fig. S1†). As shown in Fig. 2h and l, the Ru and O elements are uniformly distributed around the TiO_2 (B) nanofibers and completely overlapped on the distribution, which clearly indicates that the presence of a uniform coating layer around the TiO_2 (B) nanofibers is RuO_2, not metal Ru. In addition, the TEM image in Fig. 2g and EDX mapping of elements Ru and O in Fig. 2h and l also show that the diameter of the composition is ~350 nm. These results demonstrate that RuO_2 nanoparticles can be uniformly coated onto TiO_2 (B) nanofibers at a thickness of about 50 nm in TiO_2 (B)@ RuO_2-75 composite.

The electronic conductivities of these materials measured at the pressure of 4

MPa are also summarized in table 1. As shown in table 1, the electronic conductivity of the pristine TiO_2 (B) nanofibers powders is rather low, only 2.35×10^{-5} S cm^{-1}. However, the electronic conductivity of TiO_2 (B)@ RuO_2-75 powder (0.1 S cm^{-1}) is close to that of RuO_2 nanoparticles powder (0.2 S cm^{-1}), and is much higher than that of the pristine TiO_2 (B) nanofibers and TiO_2 (B)@ RuO_2-50 (0.01 S cm^{-1}) powders. Thereby, these results demonstrate that the uniform RuO_2-coating layer can obviously enhance the electronic conductivity of TiO_2 (B)@ RuO_2-75.

The N_2 adsorption-desorption isotherm and the pore-size distribution of pristine TiO_2 (B) nanofibers and TiO_2 (B)@ RuO_2-75 are shown Fig. 3. As shown in Fig. 3a, there is not a hysteresis loop in the nitrogen adsorption–desorption isotherm of pristine TiO_2 (B) nanofibers at relative pressure (P/P_0) of 0-0.9, suggesting no-mesopores in TiO_2 (B) nanofibers. In the nitrogen adsorption–desorption isotherm of TiO_2 (B)@ RuO_2-75 (Fig. 3b), it can be detected that a pronounced hysteresis indexed to mesopores locates in a wide relative pressure (P/P_0) range from 0.5-0.9. This result indicates that the uniformity of mesopores arises after RuO_2-coating, which is in agreement with the SEM images for TiO_2 (B)@ RuO_2-75 (see Fig. 2b). As shown in Fig. 3c**,** the pore size of pristine TiO_2 (B) nanofibers is mainly macropores with a wide size range (40–95 nm). From the pore-size distribution of TiO_2 (B)@ RuO_2-75 (Fig. 3d), it is clearly observed that there are two kinds of pores: mesopores (5–20 nm) and macropores with a wide size range (40–90 nm). These results demonstrate that the TiO_2 (B)@ RuO_2-75 composite has a typical hierarchical mesoporous/macroporous structure. The BET surface area of pristine TiO_2 (B) nanofibers and TiO_2 (B)@ RuO_2-75 is 32.2 m^2g^{-1} and 24.3 m^2g^{-1}, respectively. The lower surface area of TiO_2 (B)@ RuO_2-75 can be attributed to the dense RuO_2 coating.

In order to evaluate the effect of the cathode composition on the cycling performance of Li−O_2 cells, the TiO_2 (B)@ RuO_2-75 cathode was continuously discharged and charged for 10 cycles within a cutoff potential window from 2.0 to 4.0 V at 0.125 mA cm^{-2} (or 50 mA g^{-1}) in Fig. 4a. All of the results for the specific capacities and current densities were calculated with the total mass of TiO_2 (B)@ RuO_2-75 in the O_2 cathodes. As shown in Fig. 4a, the Li−O_2 cell with the TiO_2 (B)@ RuO_2-75 cathode exhibits rather stable specific capacities around 800 mAh g^{-1} for initial 10 cycles. Moreover, the load curves are very reproducible on cycling, except for a minor change in shape between the first charging curve and subsequent cycles, which indicates the perfect cycle performance of the Li–O_2 battery using TiO_2 (B)@ RuO_2-75 during the initial 10 cycles. In addition, Fig. 4b presents that the energy efficiencies of the Li–O_2 battery with TiO_2(B) nanofiber@ porous RuO_2 are very high (above 82.5%) over the initial 10 cycles, thus suggesting that TiO_2(B) nanofiber@ porous RuO_2 has good ORR and OER catalytic activities for the Li–O_2 battery. The TiO_2 (B) nanofibers, RuO_2 nanoparticles and TiO_2 (B)@ RuO_2-50 cathodes are also cycled at the same current density with the same test condition as TiO_2 (B)@ RuO_2-75 cathode in Fig. S4†. The Li–O_2 battery with the TiO_2 (B) nanofibers cathode displays limited capacity (~100 mAh g^{-1}) in the first discharge process. After that, this cell hardly can operate over the subsequent cycles (see Fig. S4a†). This inferior result should be attributed to the poor electronic conductivity of TiO_2 (B) nanofibers. Similarly, the reversible capacity of the TiO_2 (B)@ RuO_2-50 cathode drops rapidly during the initial 10 cycles due to the inferior electronic conductivity of the composition (Fig. S4b†). In addition, it should be noted that although the RuO_2 nanoparticles cathode exhibits a highest capacity of 915 mAh g^{-1} on the second cycles, the cycle performance of the RuO_2 nanoparticles cathode is still poor (see Fig. S4c†). Obviously, these results illustrate that RuO_2 nanoparticles have an excellent electronic conductivity and a good catalytic activity toward ORR and OER, but without stable catalyst support, the RuO_2 nanoparticles cathode displays the poor cycling performance.

Fig. 4c and d show the first discharge/charge behavior of Li-O_2 cells with TiO_2 (B)@ RuO_2-75 electrode at various current densities. As depicted in Figure 4c, the Li–O_2 battery with TiO_2 (B)@ RuO_2-75 delivers a specific discharge capacity of ~800 mAh g^{-1} at a high current density of 0.125mA cm^{-2} (or 50 mA g^{-1}). At higher current densities, the specific capacity decreases to 600 and 500 mAh g^{-1} at currents of 0.25 (or 100 mA g^{-1}) and 0.5 mA cm^{-2} (or 200 mA g^{-1}), respectively. The corresponding capacity retention is 75 and 62.5%, respectively (see Fig. 4d). The TiO_2 (B) nanofibers, RuO_2 nanoparticles and TiO_2 (B)@ RuO_2-50 cathodes are also measured at different current densities in Fig. S5†. The Li-O_2 batteries with TiO_2 (B) nanofibers cathodes and TiO_2 (B)@ RuO_2-50 cathodes both display much poor rate performance and low coulombic efficiencies (Fig. S5a and b†**)**. In addition, although the coulombic efficiencies of the RuO_2 nanoparticles cathodes are similar to these of the TiO_2 (B)@

RuO_2-75 cathodes, the rate performance of the RuO_2 nanoparticles cathodes is still inferior to that of the TiO_2 (B)@ RuO_2-75 cathodes (Fig. S5c†). These perfect performances of the TiO_2 (B)@ RuO_2-75 cathodes can be attributed to the core–shell structure, which is characterized by the excellent electronic conductivity and good catalytic activity of the typical hierarchical mesoporous/macroporous structure RuO_2 nanoparticles coating layer. Therefore, these results further confirm that TiO_2 (B)@ RuO_2-75 is a high electrocatalytic performance of cathode material for Li–O_2 batteries.

It should be noted that the cycle stability of the non-aqueous Li–O_2 batteries is generally not good at full discharge/charge condition. In response, most of reported Li–O_2 batteries were investigated with limited discharge/charge depth. According to the recently widely used capacity-limited cycle method, [6, 7, 18, 26-28, 33-35, 37-53] Fig. 5 and Fig. S6† gives the performance of these batteries investigated at fixed capacities. As shown in Fig. 5a and b, there is almost no variation in both the discharge and charge voltages of the Li–O_2 battery with TiO_2 (B)@ RuO_2-75 over 80 cycles at a fixed capacity of 300 mAh g^{-1} (with a depth of discharge of about 50%, that is, ca. 50% DOD) and a current density of 0.25 mA cm^{-2} (or 100 mA g^{-1}), indicating the perfect cycling stability of this cell. In contrast, the discharge voltages of the TiO_2 (B) nanofibers, RuO_2 nanoparticles and TiO_2 (B)@ RuO_2-50 electrodes degraded to $<$ 2.0V after only 1, 10 and 30 cycles, respectively (see Fig. S6†). We extended the battery with TiO_2 (B)@ RuO_2-75 test by determining the cycling response under higher specific capacity limits. The cycling stability of the Li–O_2 battery with TiO_2

(B)@ RuO_2-75 at the same current density of 0.25 mA cm^{-2} and a cutoff capacity of 500 mAh g^{-1} (close to 83.3% DOD) is shown in Fig. 5c and d. The discharge and charge voltages presented no decay over 25 cycles, which indicates that the TiO_2 (B)@ RuO_2-75 cathodes are highly stable at various specific capacity limits. In addition, the round-trip efficiency (the ratio of discharge to charge voltage) of the TiO_2 (B)@ RuO_2-75 cathode is much higher than these of the TiO_2 (B) nanofibers, TiO_2 (B)@ RuO_2-50 cathode and KB cathode (Fig. S7†), indicating that the discharge and charge voltages of the Li–O_2 cell can be significantly improved by the help of the uniform RuO_2 coating layer with a typical hierarchical mesoporous/macroporous structure. It can be assumed that the ordered mesopores of TiO_2 (B)@ RuO_2-75 facilitate electrolyte penetration and electron/ion transfer, and the macro-sized voids provide efficient buffer space for O_2/Li_2O_2 conversion and improve O_2 diffusion. In addition, the uniform RuO_2-coating layer alleviates undesired electrolyte and/or electrode decomposition.

To indentify the corresponding relationship between the achieved superior performance of TiO_2 (B)@ RuO_2-75 cathodes in Li–O_2 batteries and their unique structure, we collected SEM images of the TiO_2 (B)@ RuO_2-75 electrodes at different discharge-recharge stages (Fig. S8†). As shown in Fig. S8†, the Li_2O_2 nanosheets are reversibly formed and disappeared on the surface of the cathodes at the 1st cycle. Furthermore, we used *ex situ* XRD and FT-IR technologies to investigate the Li–O_2 battery before and after discharge at the first cycle. The results demonstrate the reversibility of the O_2/Li_2O_2 conversion over cycles (Fig. S9†). However, SEM investigation is not enough to clarify the reversibility of the Li–O_2 battery. Moreover, the characteristic peaks for Li_2O_2 in XRD patterns and FT-IR spectra are limited and not obvious. Therefore, these technologies are insufficient to completely characterize the products of discharge, and thus the pristine, discharged and charged TiO_2 (B)@ RuO_2-75 cathodes in the first cycle were further subjected to X-ray photoelectron spectroscopy (XPS) in Fig. 6. As shown in Fig. 6a and b, O 1s and Li 1s high-resolution XPS spectra present peaks at a binding energy of 531.2 eV and 54.8 eV for the TiO_2 (B)@ RuO_2-75 discharged electrodes, respectively, which indicates a large amount of Li_2O_2 generated in the discharging process. After charged, the characteristic peaks of Li_2O_2 in the O 1s and Li 1s XPS spectra are completely decomposed, demonstrating the reversible conversion between O_2 and Li_2O_2. When switched to the C 1s XPS spectra in Fig. 6c, a small number of Li_2CO_3 can be found in the TiO_2 (B)@ RuO_2-75 discharged cathode, and then all of them can be decomposed in the recharging process. In addition, the characteristic peaks corresponding to RuO_2 and TiO_2 in the Ru 3d and Ti 2p XPS spectra can be detected in the pristine, discharged and recharged TiO_2 (B)@ RuO_2-75 cathodes. However, the intensity of the peaks assigned to RuO_2 and TiO_2 in the Ru 3d and Ti 2p XPS spectra in the discharged TiO_2 (B)@ RuO_2-75 cathode is obviously reduced, compared with these in the pristine and recharged cathodes (Fig. 6c and d). This phenomenon can be ascribed to the surface of the discharged cathodes filled with discharge products, in agreement with the SEM images in Fig. S8†. Thereby, these results suggest that the TiO_2 (B)@ RuO_2-75 cathodes are stable against the highly reactive intermediate species attack and can support stable and reversible Li_2O_2 formation/decomposition in contact with a DMSO electrolyte during cycles.

To further confirm that the reaction at the TiO_2 (B)@ RuO_2-75 cathode is overwhelmingly Li_2O_2 formation/decomposition, *in situ* differential electrochemical mass spectrometry (DEMS) is employed to measure the gas evolution during charging. The DEMS system was built in-house and guided by the requirement to detect the gases evolved during the charge process. A quadrupole mass spectrometer with leak inlet is connected to a customized Swagelok cell assembly (see Fig. S10†). Each tested cell was discharged with a fixed capacitance of 500 mAh g^{-1} in the sealed assembly at a current density of 0.125 mA cm^{-2}, and then online gas analysis was performed during the recharge with a purge Ar stream at a current density of 0.25 mA cm^{-2} with a fixed capacity of 500 mAh g^{-1}. Before the recharge test and online gas analysis, the system was purged with pure Ar stream for 12 hours, and the background for O_2 and CO_2 was calibrated. Fig. 7a presents the charge curve of Li–O_2 battery using the TiO_2 (B)@ RuO_2-75 cathode and corresponding gas evolution analysis. As shown in Fig. 7a, O_2 is evolved dominantly during the recharge process, and there is only very small CO_2 evolved during charging at a current of 0.25 mA cm^{-2} under Ar, confirming that the decomposition of Li_2O_2 dominates charge process. The O_2/Li_2O_2 conversion in KB cathode was also investigated by in-situ DEMS at the same condition for comparison (Fig. 7b). Although the O_2 evolution also dominates the charge in KB cathode (Fig. 7b), its CO_2 evolution over recharge process is much more obvious than that in the TiO_2 (B)@ RuO_2-75 cathode. In addition, charge overpotential for the TiO_2 (B)@ RuO_2-75 cathode is obvious lower than that of KB cathode (see red dashed for comparison), which indicates the RuO_2 coating layer can function as an efficient OER catalyst in Li−O_2 cells. Furthermore, the evolution of CO_2 from the TiO_2 (B)@ RuO_2-75 cathode is attributed to the limited amount of Li_2CO_3 generated in the discharging process, which is in good correspondence with the XPS spectra. The Li_2CO_3 generated on the TiO_2 (B)@ RuO_2-75 cathode should be derived from the decomposition of electrolyte because it is the only carbon source. Currently, the instability of electrolytes remains a great challenge for Li−O_2 cells.

According to previous reports, [55-57] ruthenium oxide (RuO_2) has been identified as an electrode material for lithium ion battery in the conventional organic carbonate based electrolytes with favorable characteristics, such as high chemical and thermal stability and potential for high capacity. Furthermore, Ru- and RuO_2-based materials have been widely used as cathode catalysts for Li−O_2 battery in ether [37, 39, 40, 46,48,50,53] or DMSO[38] based electrolytes. However, the lithiation/de-lithiation performance of Ru- or RuO_2-based materials in ether or DMSO based electrolytes is rarely reported. Therefore, the lithiation/de-lithiation performance of TiO_2 (B)@ RuO_2-75 is further investigated in DMSO-(0.1M) $LiClO_4$ electrolyte. Fig. 8 displays the galvanostatic charge–discharge profiles of the sealed Li–TiO_2 (B)@ RuO_2-75 cell in DMSO-(0.1M) $LiClO_4$ electrolyte with the potential window from 2.0 to 4.3 V as the cutoff values at a current density of 0.125 mA cm^{-2} during the initial 10 cycles. All of the results for the specific capacities and current densities were calculated with the total mass of TiO_2 (B)@ RuO_2-75 in the cathodes. As shown in Fig. 8, the cell exhibits rather stable specific capacities above130–140 mAh g^{-1} and its charge/discharge profiles are reproducible, with no sign of deterioration for 10 cycles, which indicates a perfect cycling performance. Furthermore, it is worth noting that some discharge capacity (~ 100 mAh/g) can be observed above 3 V for the Li–O_2 battery with TiO_2 (B)@ RuO_2-75 in Fig. 4 and Fig. 5. This interesting result demonstrates that the reversible lithiation/de-lithiation of RuO_2 can contribute capacity for the Li–O_2 battery with TiO_2 (B)@ RuO_2-75 over charge/discharge process. On the other hand, the reversible lithiation/de-lithiation of RuO_2 in the TiO_2 (B)@ RuO_2-75 cathodes may be also one of factors for the achieved high efficiency of the Li-O_2 batteries.

Conclusion

In summary, a RuO_2 nanoparticles shell uniformly coated on the surface of core TiO_2 (B) nanofibers by a simple sol–gel method, and the resulting composite was applied as a catalyst for Li−O_2 batteries. The composite TiO_2 (B) nanofiber@ porous RuO_2 demonstrates bifunctional catalytic activity for both the ORR and the OER in Li–O_2 batteries. With the high mass loading of 2.5 mg cm^{-2} on the electrode, the Li−O_2 cells composed of TiO_2 (B)@ RuO_2-75 cathodes show both perfect capacity retention (~800 mAh g^{-1} within a potential window from 2.0 to 4.0 V for 10 cycles with little capacity decay and few potential variations at 0.125 mA cm^{-2}) with a very high energy efficiency of >82.5%, and good rate performance (500 mAh g^{-1} at 0.5 mA cm^{-2}, which is about 62.5% of that at 0.125 mA cm^{-2}) at full discharge/charge condition. When cycled with limited capacity of 300 mAh g^{-1}, the cell delivers not only high round-trip efficiency but also long cycle life (80 cycles). Furthermore, the discharge and charge potentials of the Li–O_2 battery show almost no change over 25 cycles with a fixed capacity of 500 mAh g^{-1} at a current of 0.25 mA cm^{-2}. This excellent performance can be ascribed to the typical hierarchical mesoporous/macroporous structure in TiO_2 (B)@ RuO_2-75 composites which can not only facilitate electrolyte penetration and electron/ion transfer, but also provide efficient buffer space for O_2/Li_2O_2 conversion and improve O_2 diffusion, and the uniform RuO_2 coating layer which could alleviate undesired electrolyte and/or electrode decomposition and also improve the surface electronic conductivity of TiO_2 (B)@ RuO_2-75 composites. In addition, we also use a combination of *ex situ* SEM, FTIR, PXRD, XPS and *in situ* DEMS measurements to further demonstrate that the TiO_2 (B)@ RuO_2-75 cathodes are stable against the highly reactive intermediate species attack and can support stable and reversible Li_2O_2 formation/decomposition in contact with a DMSO-based electrolyte during cycles. Furthermore, we also find that some discharge capacity (~100 mAh/g) observed above 3 V for the Li–O_2 battery with TiO_2 (B)@ RuO_2-75 can be attributed to the lithiation/de-lithiation of RuO_2. This interesting result also indicates that the battery with TiO_2 (B)@ RuO_2-75 can also be operated as a rechargeable RuO_2/Li battery without O_2 in environment. We hope that these results presented here would encourage further studies of cathode design in Li–O_2 batteries, although the electrolyte is still challenges for realizing practical devices. Therefore, further studies should be focused on the development of stable electrolytes.

Acknowledgements

The authors acknowledge funding support from the Natural Science Foundation of China (21373060, 21103025), the State Key Basic Research Program of PRC (2014CB932301), Shanghai Pujiang Program (13PJ1400800), and Shanghai Science & Technology Committee (11DZ1100207, 08DZ2270500).

References

1. D. G. Kwabi, N. Ortiz-Vitoriano, S. A. Freunberger, Y. Chen, N. Imanishi, P. G. Bruce and Y. Shao-Horn, *MRS Bulletin*, 2014, **39**, 443-452.
2. L. Grande, E. Paillard, J. Hassoun, J. B. Park, Y. J. Lee, Y. K. Sun, J. Passerini and B. Scrosati, *Adv. Mater.*, 2015, **27**, 784-780.
3. J.-S. Lee, S.T. Kim, R. Cao, N.S. Choi, M. Liu, K.T. Lee and J. Cho, *Adv. Energy Mater.*, 2011, **1**, 34-50.
4. Y. Y. Shao, F. Ding, J. Xiao, J. Zhang, W. Xu, S. Park, J.-G. Zhang, Y. Wang and J. Liu, *Adv. Funct. Mater.*, 2013, **23**, 987-1004.
5. K. M. Abraham and Z. Jang, *J. Electrochem. Soc.*, 1996, **143**, 1-5.
6. S. H. Oh, R. Black, E. Pomerantseva, J.-H. Lee and L. F. Nazar, *Nat. Chem.*, 2012, **4**, 1004-1010.
7. H.-G. Jung, J. Hassoun, J.-B. Park, Y.-K. Sun and B. Scrosati, *Nat. Chem.*, 2012, **4**, 579-585.
8. Z. Peng, S. A. Freunberger, Y. Chen and P. G. Bruce, *Science*, 2012, **337**, 563-566.
9. M. M. O. Thotiyl, S. A. Freunberger, Z. Q. Peng, Y. H. Chen, Z. Liu and P. G. Bruce, *Nat. Mater.*, 2013, **12**, 1049-1055.
10. N. B. Aetukuri, B. D. McCloskey, J. M. Garcia, L. E. Krupp, V. Viswanathan

and A. C. Luntz, *Nat. Chem.*, 2015, **7**, 50-56.

11. L. Johnson, C. M. Li, Z. Liu, Y. H. Chen, S. A. Freunberger, P. C. Ashok, B. B. Praveen, K. Dholakia, J.-M. Tarascon and P. G. Bruce, *Nat. Chem.*, 2014, **6**, 1091-1099.
12. G. Girishkumar, B. McCloskey, A. Luntz, S. Swanson and W. Wilcke, *J. Phys. Chem. Lett.*, 2010, **1**, 2193-2203.
13. F. J. Li, T. Zhang and H. S. Zhou, *Energy Environ. Sci.*, 2013, **6**, 1125-1141.
14. B. D. McCloskey, D. S. Bethune, R. M. Shelby, G. Girishkumar and A. C. Luntz, *J. Phys. Chem. Lett.*, 2011, **2**, 1161-1166.
15. W. Xu, J. Z. Hu, M. H. Engelhard, S. A. Towne, J. S. Hardy, J. Xiao, J. Feng, M. Y. Hu, J. Zhang, F. Ding, M. E. Gross and J.-G. Zhang, *J. Power Sources*, 2012, **215**, 240-247.
16. B. D. McCloskey, A. Speidel, R. Scheffler, D. C. Miller, V. Viswanathan, J. S. Hummelshøj, J. K. Nørskov and A. C. Luntz, *J. Phys. Chem. Lett.*, 2012, **3**, 997-1001.
17. V. S. Bryantsev, J. Uddin, V. Giordain, W. Walker, D. Addison and G. V. Chase, *J. Electrochem. Soc.*, 2013, **160**, A160-A171.
18. Z.Y. Guo, G. N. Zhu, Z. Qiu, Y. G. Wang and Y.Y. Xia, *Electrochem. Commun.*, 2012, **25**, 26-29.
19. V. S. Bryantsev, V. Giordani, W. Walker, M. Blanco, S. Zecevic, K. Sasaki, J. Uddin, D. Addison and G. Chase, *J. Phys. Chem. A*, 2011, **115**, 12399-12409.
20. B. M. Gallant, R. R. Mitchell, D. G. Kwabi, J. G. Zhou, L. Zuin, C. V.

Thompson and Y. Shao-Horn, *J. Phys. Chem. C*, 2012, **116**, 20800-20805.

21. W. Walker, V. Giordani, J. Uddin, V. S. Bryantsev, G. Chase and D. Addison, *J. Am. Chem. Soc.*, 2013, **135**, 2076-2079.
22. S. A. Freunberger, Y. H. Chen, Z. Q. Peng, J. M. Griffin, L. J. Hardwick, F. Barde, P. Novak and P. G. Bruce, *J. Am. Chem. Soc.*, 2011, **133**, 8040-8047.
23. Y. Chen, S. A. Freunberger, Z. Peng, F. Barde, P. G. Bruce, *J. Am. Chem. Soc.* **2012**, *134*, 7952-7957.
24. R. Black, S. H. Oh, J. H. Lee, T. Yim, B. Adams and L. F. Nazar, *J. Am. Chem. Soc.*, 2012, **134**, 2902-2905.
25. J. Xiao, D. H. Mei, X. L. Li, W. Xu, D.Wang, G. L. Graff, W. D. Bennett, Z. Nie, L. V. Saraf, I. A. Aksay, J. Liu and J. G. Zhang, *Nano Lett.*, **2011**, *11*, 5071-5078.
26. J. J. Xu, Z. L.Wang, D. Xu, L. L. Zhang and X. B. Zhang, *Nat. Commun.*, 2013, **4**, 2438.
27. Z. Y. Guo, D. D. Zhou, X. L. Dong, Z. J. Qiu, Y. G.Wang and Y. Y. Xia, *Adv. Mater.*, 2013, **25**, 5668-5672.
28. J. J. Xu, D. Xu, Z. L. Wang, H. G. Wang, L. L. Zhang and X. B. Zhang, *Angew. Chem. Int. Ed.*, 2013, **52**, 3887-3890.
29. J. Lu, Y. Lei, K. C. Lau, X. Luo, P. Du, J. Wen, R. S. Assary, U. Das, D, Miller, J. W. Elam, H. M. Albishri, D. A. El-Hady, Y. K. Sun, L. A. Curtiss and K. Amine, *Nat. Commun.*, 2013, **4**, 2255.
30. J.-L. Shui, J. S. Okasinski, P. Kenesei, H. A. Dobbs, D. Zhao, J. D. Almer and D.-J. Liu, *Nat. Commun.*, 2013, **4**, 2255.

31. H. D. Lim, H. Song, J. Kim, H. Gwon, Y. Bae, K. Y. Park, J. Hong, H. Kim, T. Kim, Y. H. Kim, X. Lepro, R. Ovalle-Robles, R. H. Baughman and K. Kang, *Angew. Chem. Int. Ed.*, 2014, **53**, 3926-3931.
32. M. M. O. Thotiyl, S. A. Freunberger, Z. Peng and P. G. Bruce, *J. Am. Chem. Soc.*, 2013, **135**, 494-500.
33. T. Zhang and H. S. Zhou, *Nat. Commun.*, 2013, **4**, 1817.
34. Z. Y. Guo, J. Wang, F. Wang, D. D. Zhou, Y. Y. Xia and Y. G. Wang, *Adv. Funct. Mater.*, 2013, **23**, 4840-4846.
35. Y. G. Wang and H.S. Zhou, *J. Power Sources*, 2010, **195**, 358-361.
36. Y. Li, J. Wang, X. Li, D. Geng, M. N. Banis, Y. Tang, D. Wang, R. Li, T.-K. Sham and X. L. Sun, *J. Mater. Chem.*, 2012, **22**, 20170-20174.
37. Z. L. Jian, P. Liu, F. J. Li, P. He, X. W. Guo, M. W. Chen and H. S. Zhou, *Angew. Chem. Int. Ed.*, 2014, **53**, 442-446.
38. B. Sun, X.D. Huang, S.Q. Chen, P. Munroe and G. X. Wang, *Nano Lett.*, 2014, **14**, 3145-3152.
39. H. G. Jung, Y. S. Jeong, J. B. Park, Y. K. Sun, B. Scrosati and Y. J. Lee, *ACS Nano*, 2013, **7**, 3532-3539.
40. Z.Y. Guo, D. D. Zhou, H. J. Liu, X. L. Dong, Y. S. Yi, A. S. Yu, Y. G. Wang and Y.Y. Xia, *J. Power Sources*, 2015, **192**, 181-188.
41. X. Huang, B. Sun, D. Sun, D. Y. Zhao and G. X. Wang, *J. Mater. Chem. A*, 2014, **2**, 7973-7979.
42. R. R. Mitchell, B. M .Gallant, C. V. Thompson and Y. Shao-Horn, *Energy*

Environ. Sci., 2011, **4**, 2952-2958.

43. Y. Hu, T. Zhang, F. Cheng, Q. Zhao, X. Han and J. Chen, *Angew. Chem. Int. Ed.*, 2015, **54**, 4338-4343.
44. S. H. Oh and L. F. Nazar, *Adv. Energy Mater.*, 2012, **2**, 903.
45. H. Wang, Y. Yang, Y. Liang, G. Zheng, Y. Li, Y. Cui and H. Dai, *Energy Environ. Sci.*, 2012, **5**, 7931-7935.
46. F. J. Li D. M. Tang, Y. Chen, D. Golberg, H. Kitaura, T. Zhang, A.Yamada and H. S. Zhou, *Nano Lett.*, 2013, **13**, 4702-4707.
47. H. Lee, Y. Kim, D. Lee, J. Song, Y. M. Lee, H. T. Kim and J. K. Park, *J. Mater. Chem. A*, 2014, **2**, 11891-11898.
48. F. J. Li D. M. Tang, Z. L. Jian, D. Liu, D. Golberg, A.Yamada and H. S. Zhou, *Adv. Mater.*, 2014, **26**, 4659-4664.
49. A. Riaz, K. N. Jung, W. Chang, K. H. Shin and J. W. Lee, *ACS Appl. Mater. Interfaces*, 2014, **6**, 17815-17822.
50. K. Liao, T. Zhang, Q. Wang, F. Li, Z. Jian, H. Yu and H. S. Zhou, *ChemSusChem*, 2015, 8, 1429-1434.
51. G. Zhao, R. Mo, B. Wang, L. Zhang and K. Sun, *Chem. Mater.*, 2014, **26**, 2551-2556.
52. A. Riaz, K. N. Jung, W. Chang, S. B. Lee, T. H. Lim, S. J. Park, R. H. Song, S. Yoon, K. H. Shin and J. W. Lee, *Chem. Commun.*, 2013, 49, 5984-5986.
53. G. Zhao, Y. Niu, L. Zhang and K. Sun, *J. Power Sources*, 2014, **270**, 386-390.
54. Z. Y. Guo, X. L. Dong, D. D. Zhou, Y. J. Du, Y. G. Wang, Y. Y. Xia, *RSC Adv.*

2013, *3*, 3352-3358.

55. A. S. Hassan, A. Navulla, L. Meda, B. R. Ramachandran and C. D. Wick, *J. Phys. Chem. C*, 2015, **119***,* 9705-9713.
56. J. Jung, M. Cho and M. Zhou, *AIP Adv.*, 2014, **4**, 017104−1-12.
57. P. Balaya, H. Li, L. Kienle, J. Maier and J. Fully, *Adv. Funct. Mater.*, 2003, **13**, 621-625.

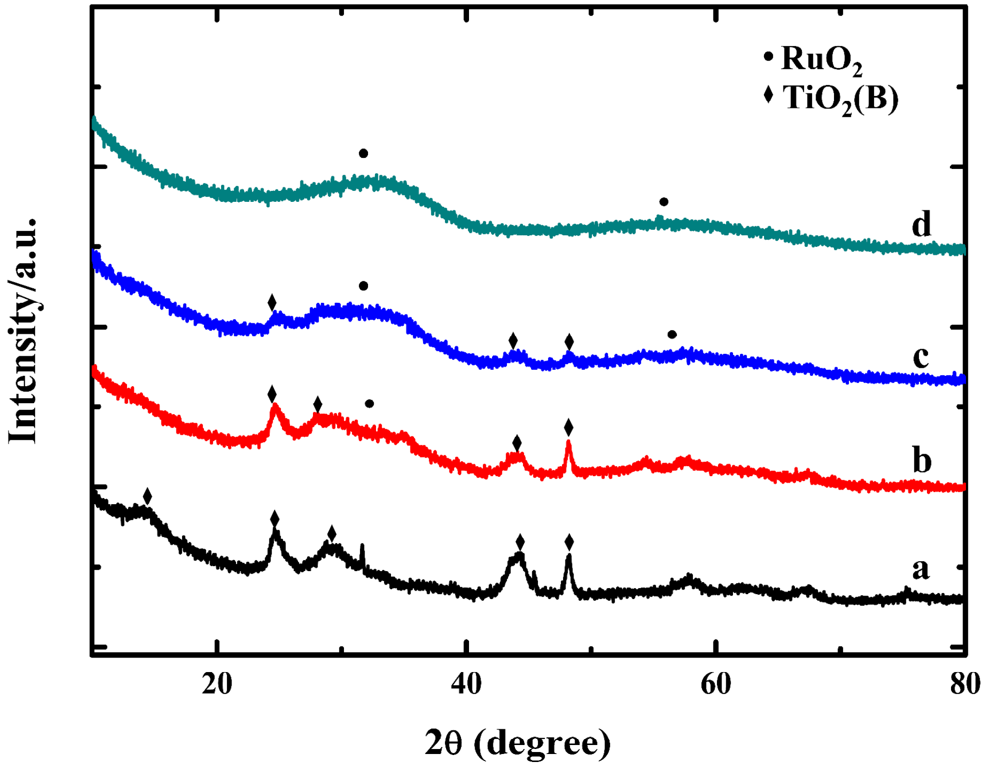

Fig. 1 XRD patterns of the as-prepared samples: (a) TiO_2 (B) nanofibers; (b) TiO_2 (B)@ RuO_2-50; (c) TiO_2 (B)@ RuO_2-75; (d) RuO_2 nanoparticles.

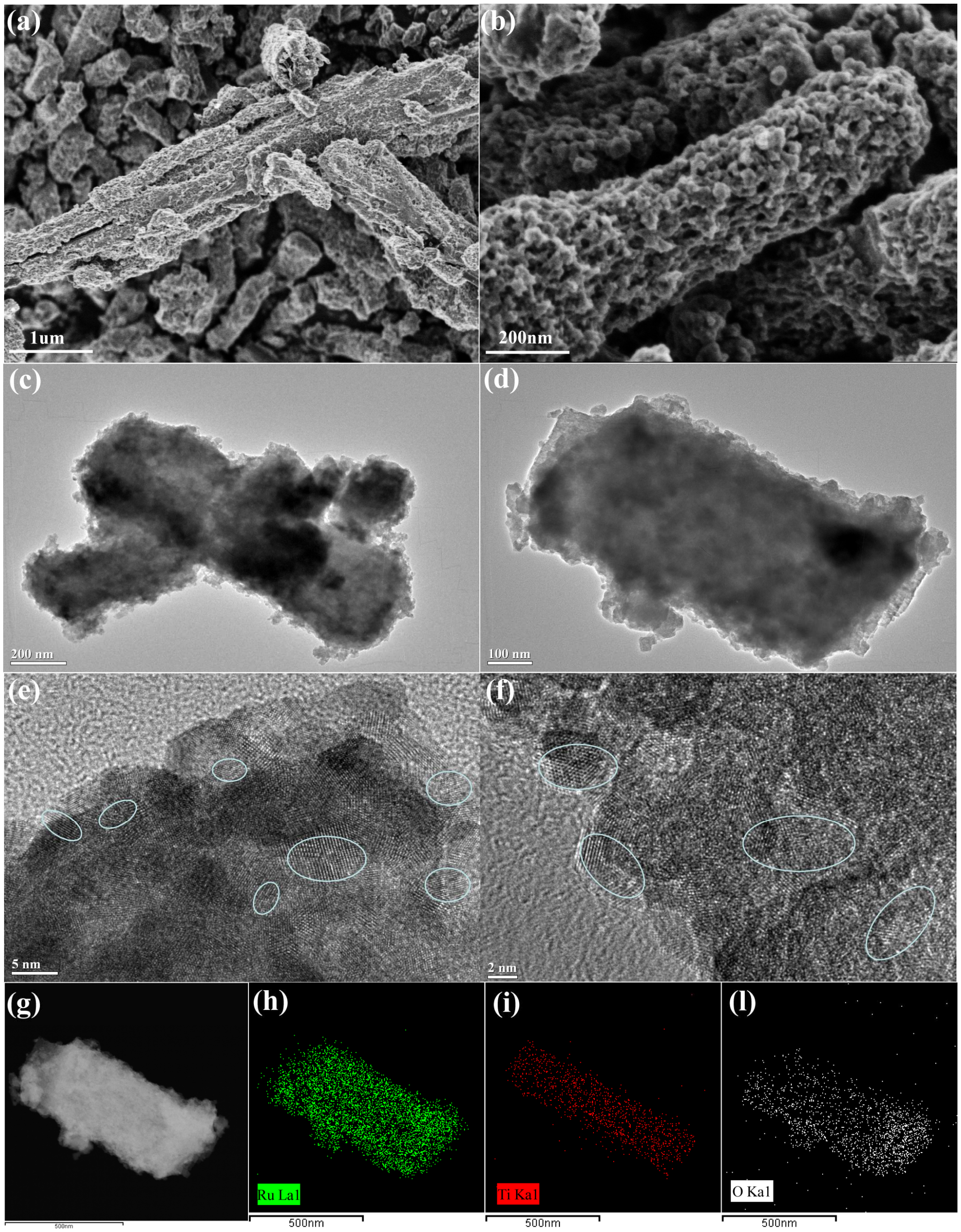

Fig. 2 (a~b) SEM images and (c~f) TEM images of TiO_2 (B)@ RuO_2-75 with different magnifications. (g) TEM image of TiO_2 (B)@ RuO_2-75 (bottom left) and (h~l) the corresponding EDX mapping images of Ru, Ti and O elements.

Materials	TiO_2 (B) nanofibers	TiO_2 (B)@ RuO_2-50	TiO_2 (B)@ RuO_2-75	RuO_2 nanoparticles
Conductivity (S/cm)	2.35×10^{-5}	0.01	0.1	0.2

Table 1 Electronic conductivities of TiO_2 (B) nanofibers, TiO_2 (B)@ RuO_2-50, TiO_2 (B)@ RuO_2-75 and RuO_2 nanoparticles powders measured at a pressure of 4MPa.

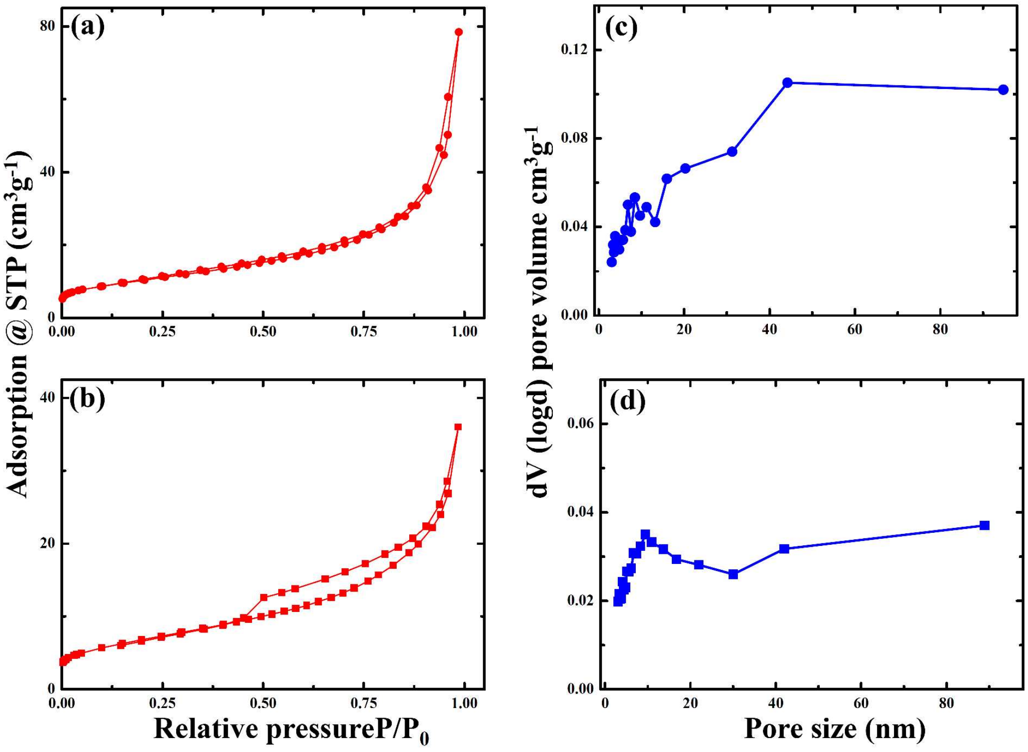

Fig. 3 Nitrogen adsorption-desorption isotherms and pore-size distribution of TiO_2 (B) nanofibers (a, c) and TiO_2 (B)@ RuO_2-75 (b, d).

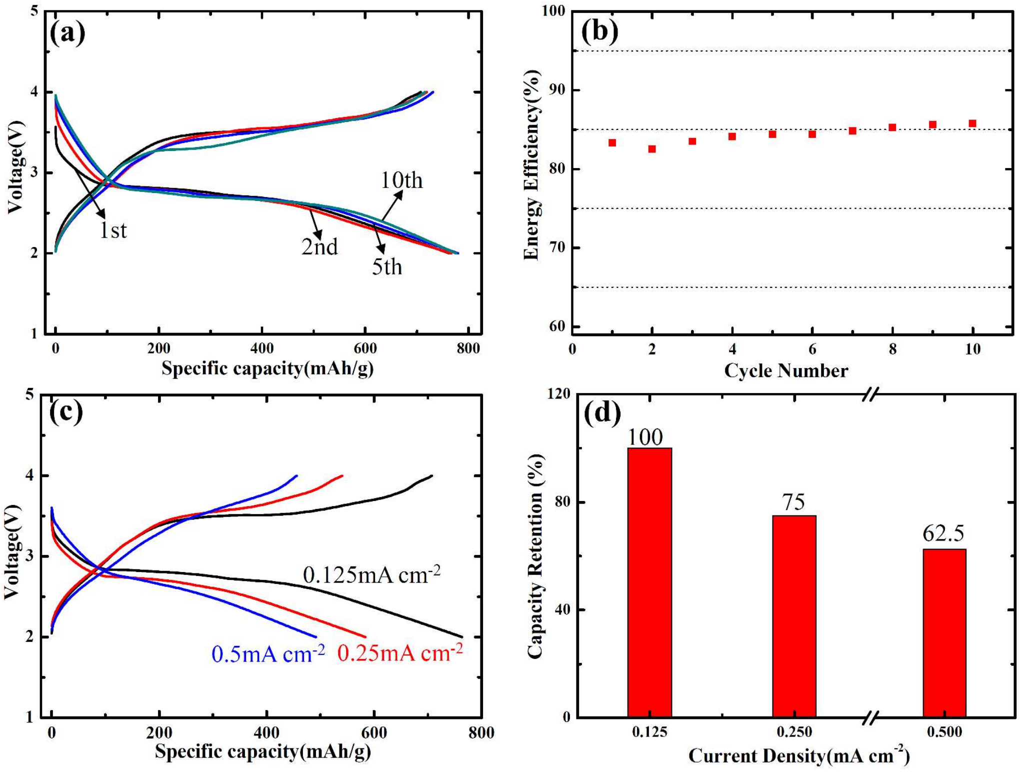

Fig. 4 (a) The discharge/charge curves of the Li−O_2 batteries using TiO_2 (B)@ RuO_2-75 in porous catalytic electrode for initial 10 cycles at a current density of 0.125 mA cm^{-2} with the voltage window of 2V~4.0V. (b) The corresponding energy efficiencies over the initial 10 cycles. The discharge/charge curves (c) and capacity retention capability (d) of the Li−O_2 batteries with TiO_2 (B)@ RuO_2-75 at different applied current densities. (All of the results for the specific capacities and current densities are calculated with the total mass of TiO_2 (B)@ RuO_2-75 in the O_2 cathodes.)

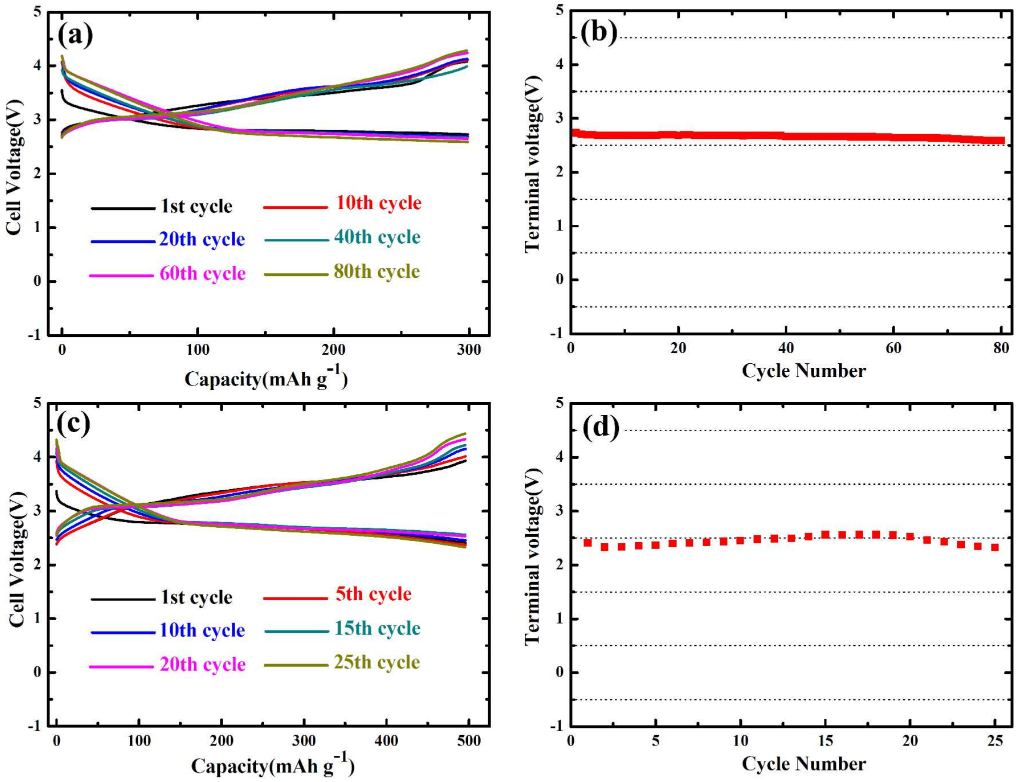

Fig. 5 (a) Discharge–charge curves and (b) Variation of voltage on the terminal of discharge of the Li–O_2 cell with TiO_2 (B)@ RuO_2-75 cathode during different cycles at a current density of 0.25 mA cm^{-2} with a fixed capacity of 300 mAh g^{-1}; Cycle performance of the TiO_2 (B)@ RuO_2-75 cathodes at a current density of 0.25 mA cm^{-2} with a fixed capacity of 500 mAh g^{-1}: (c) The discharge/charge curves at different cycles and (d) voltage on the terminal of discharge vs. cycle number.

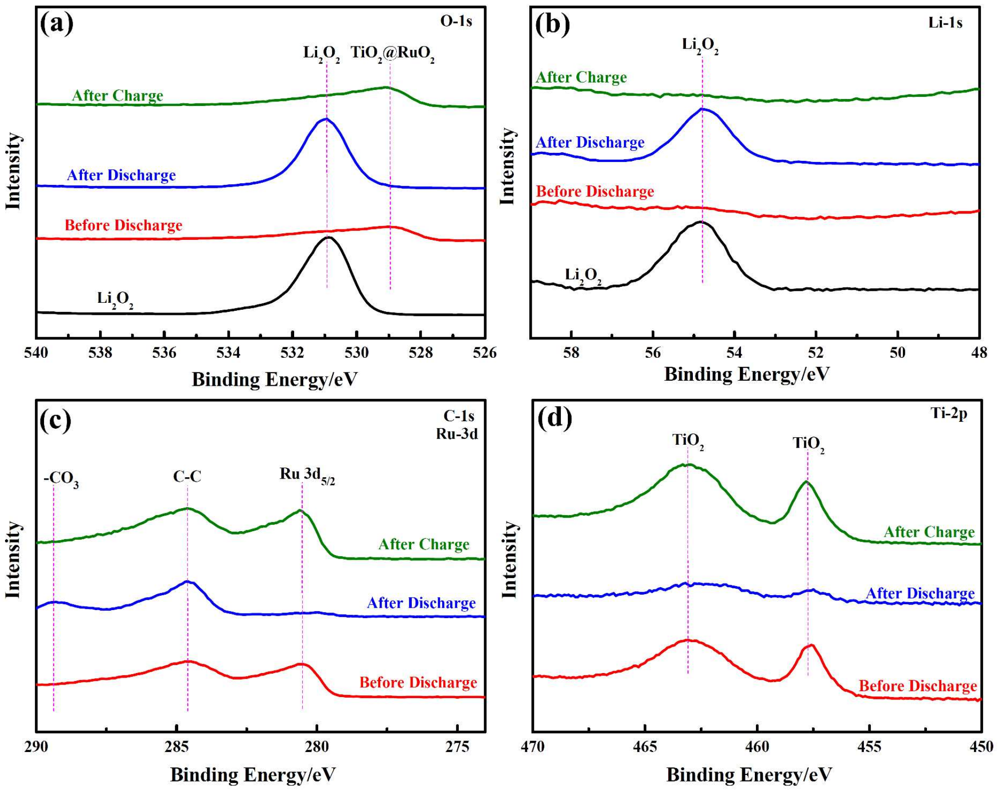

Fig. 6 (a) O 1s, (b) Li 1s, (c) C1s & Ru 3d and (d) Ti 2p XPS spectra of the pristine discharged and charged TiO_2 (B)@ RuO_2-75 cathodes.

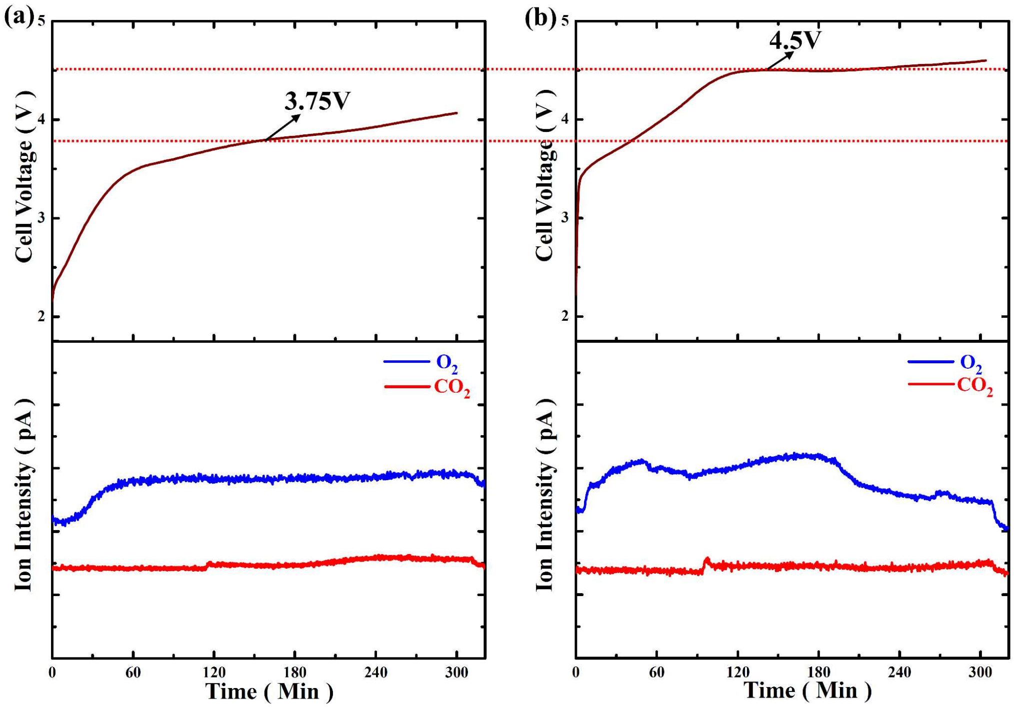

Fig. 7 (a) Gas evolution and corresponding charge curve at a current density of 0.25 mA cm^{-2} of Li–O$_2$ battery using TiO$_2$ (B)@ RuO$_2$-75 cathode with a fixed capacity of 500 mAh g^{-1}. (b) Gas evolution and corresponding charge curve at a current density of 0.25 mA cm^{-2} of Li–O$_2$ battery using bare KB cathode with a fixed capacity of 500 mAh g^{-1}.

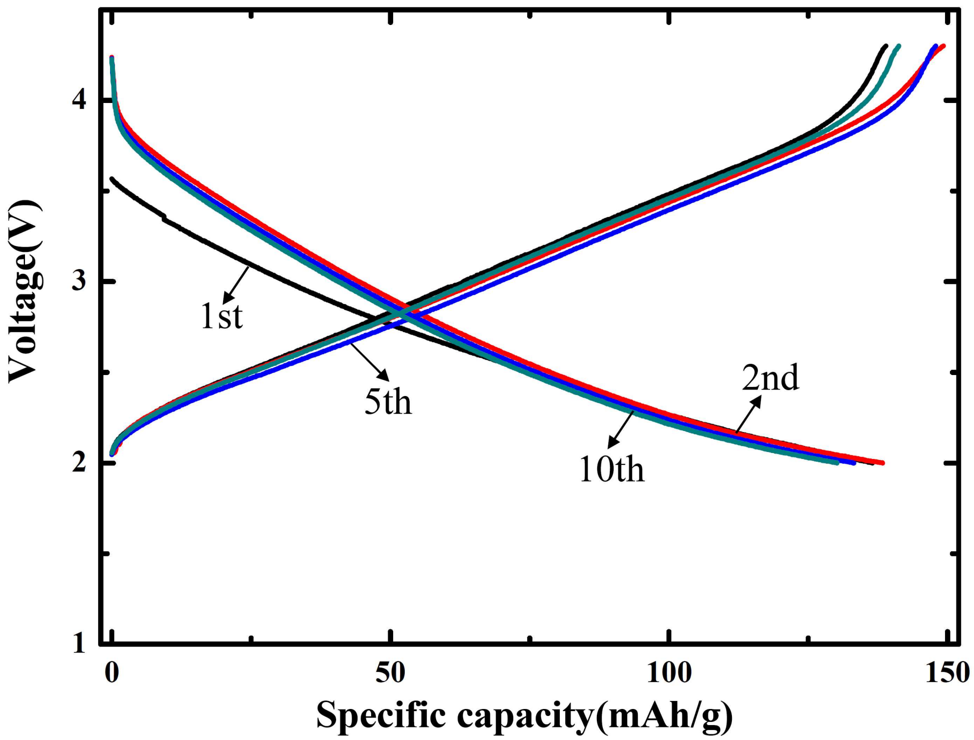

Fig. 8 Galvanostatic discharge/charge curves for the initial 10 cycles of the as-prepared TiO_2 (B)@ RuO_2-75 electrode in lithium half-cell between 2 and 4.3 V at a current density of 0.125mA cm^{-2}.

A Core–Shell-Structured TiO_2 (B) nanofiber @ porous RuO_2 Composite as a Carbon-Free Catalytic Cathode for Li−O_2 Battery

Ziyang Guo, Chao Li, Jingyuan Liu, Xiuli Su, Yonggang Wang* and Yongyao Xia

Table of Contents

We designed a core-shell-structured TiO_2 (B) nanofiber@ porous RuO_2 composite as a carbon-free cathode for Li–O_2 battery.

TOC Figure